

Far-Infrared Laser Magnetic Resonance Spectroscopic Study of the ν_2 Bending Fundamental of the CCN Radical in Its $\tilde{X}^2\Pi_r$ State

Michael D. Allen,^{*1} Kenneth M. Evenson,^{*} David A. Gillett,[†] and John M. Brown[‡]

^{*}National Institute of Standards and Technology, Time and Frequency Division 847, 325 Broadway, Boulder, Colorado 80303; [†]Lambda Physik GmbH, Hansböcklerstr. 12, D37079, Göttingen, Germany; and [‡]Physical and Theoretical Chemistry Laboratory, South Parks Road, Oxford OX1 3QZ, United Kingdom

Received October 22, 1999; in revised form January 24, 2000

Bending vibration–rotation transitions between the (010) $\mu^2\Sigma^-$ and (000) $^2\Pi_r$ vibronic states of the CCN radical in its ground electronic state have been observed using far-infrared laser magnetic resonance (FIR LMR) spectroscopy. Thirteen FIR laser lines were used to record 769 resonances. The LMR data, combined with previous data, were used to determine vibrational, Renner–Teller, fine-structure, rotational, hyperfine, and molecular g -factor parameters using a least-squares fitting routine. The model used was an N^2 effective Hamiltonian modified to include the Renner–Teller effect explicitly in a $^2\Pi$ electronic state. The band origin for the (010) $\mu^2\Sigma^- \leftarrow$ (000) $\tilde{X}^2\Pi_r$ transition was determined to be 179.598176 ± 0.000067 cm^{-1} . The spin–orbit splitting in the ground state was refined and the complete set of ^{14}N -hyperfine parameters determined for the first time.

Key Words: FIR LMR; bending vibrational transitions; Renner–Teller effect.

INTRODUCTION

Merer and Travis (1) made the first spectroscopic observation of CCN in 1965. Since then, this free radical has been the subject of numerous experimental and theoretical investigations (2–16). One of the main reasons for studying CCN is its astrophysical importance. Many carbon-containing and more specifically carbon-chain species have been detected in stellar and interstellar objects (2). So far, observations of CCN have not been successful, although the molecular constants and predictions for the ground state are very accurate (14). Another very important reason for the continued interest in CCN is that it exhibits the Renner–Teller effect, which is the coupling between the bending vibrational and electronic orbital angular momenta. This interaction poses difficult problems for both theoreticians and experimentalists. Pople (17) was the first to work out the mathematical details needed to calculate the vibronic energy levels for a nonrotating triatomic molecule in a $^2\Pi$ state. Soon afterwards, Hougen (18) added to this by working out the energy level expressions for a rotating triatomic molecule in a $^2\Pi$ state. The work by Merer and Travis laid the groundwork for understanding the electronic structure of CCN. They observed the absorption spectra of the $\tilde{A}^2\Delta_i \leftarrow \tilde{X}^2\Pi_r$, $\tilde{B}^2\Sigma^- \leftarrow \tilde{X}^2\Pi_r$, and $\tilde{C}^2\Sigma^+ \leftarrow \tilde{X}^2\Pi_r$ electronic transitions. From these measurements, they determined rotational, fine-structure, and some vibrational parameters for CCN. In

addition, they observed the Renner–Teller effect in a $^2\Delta$ electronic state for the first time.

Since the work by Merer and Travis, there have been several subsequent studies of the $\tilde{A}^2\Delta_i \leftarrow \tilde{X}^2\Pi_r$ transition (3–7, 11) and one of the $\tilde{C}^2\Sigma^+ \leftarrow \tilde{X}^2\Pi_r$ transition (15). Kakimoto and Kasuya (3) were able to improve upon the molecular parameters determined for the zero-point levels of both the $\tilde{X}^2\Pi_r$ and $\tilde{A}^2\Delta_i$ electronic states. Hakuta and Uehara (4) used an Ar⁺ laser to pump the CCN radical into the $\tilde{A}^2\Delta_i$ state and observed the resulting LIF. From these measurements, they were able to determine vibrational and vibronic parameters for CCN in the $\tilde{X}^2\Pi_r$ state. Bernath and co-workers (5, 6) reported two studies of the $\tilde{A}^2\Delta_i \leftarrow \tilde{X}^2\Pi_r$ transition. They were able to determine rotational constants for CCN in several vibronic levels and, more importantly, they determined the Renner–Teller and other vibrational parameters in the ground state (5). In a similar study to that of Kakimoto and Kasuya on the (000)–(000) transition, Kawaguchi *et al.* (7) recorded the hot bands (010)–(010) and (020)–(020) in the $\tilde{A}^2\Delta_i \leftarrow \tilde{X}^2\Pi_r$ transition. The work by Kawaguchi *et al.* (7) determined many important spectroscopic parameters for several vibronic levels in both the $\tilde{A}^2\Delta_i$ and $\tilde{X}^2\Pi_r$ states. In addition, there have been microwave studies of CCN in both the $\tilde{X}^2\Pi_{1/2}$ (14) and the $\tilde{A}^2\Delta_i$ (8) states where hyperfine structure was resolved and analyzed. Bondybey and English (9) were able to observe CCN at low temperatures trapped in an argon matrix where they determined values for ν_1 and ν_3 and estimated a value for ν_2 . Jacox (10) was also successful in observing CCN in a low-temperature matrix. More recently, studies of the ν_1 band in the ground electronic state with diode-laser (12) and CO LMR (13) techniques have

Supplementary data for this article are available on the journal home page (<http://www.academicpress.com/jms>) and as part of the Ohio State University Molecular Spectroscopy Archives (http://msa.lib.ohio-state.edu/jmsa_hp.htm).

¹ National Research Council Postdoctoral Fellow.

been reported further improving the molecular parameters. The most recent paper was by Kohguchi *et al.* (15) on the $\tilde{C}^2\Sigma^+ \leftarrow \tilde{X}^2\Pi_r$ transition. Their study was only the second of this transition after the first observation by Merer and Travis. They were able to observe progressions in all three of the vibrational modes and determined molecular parameters for CCN in the $\tilde{C}^2\Sigma^+$ state. Moreover, they were able to construct the vibronic structure for the ground electronic state and determine several vibronic parameters including the Renner parameter using expressions derived by perturbation theory.

This paper reports the first direct measurement of the ν_2 bending vibrational transition, (010) $\mu^2\Sigma^- \leftarrow (000) \tilde{X}^2\Pi_r$, and the most complete and accurate set of molecular parameters for the (000) $\tilde{X}^2\Pi_r$ and (010) $\mu^2\Sigma^-$ vibronic states. The data were analyzed explicitly using an N^2 Hamiltonian modified to include the Renner–Teller interaction for a $^2\Pi$ state. This method of analysis is more reliable than the use of expressions derived from perturbation theory, which become unreliable when the Renner parameter ϵ is large (0.418 for CCN). The data set includes observations from the present study of the FIR LMR spectrum, microwave data of CCN in the $\tilde{X}^2\Pi_{1/2}$ state reported by Ohshima and Endo (14), spin-orbit transition data (3, 7), and vibronic transition data (1, 15). The spin-orbit data were calculated from differences between two rovibronic lines in the $\tilde{A}^2\Delta_i \leftarrow \tilde{X}^2\Pi_r$ electronic transition that share the same upper state, but have different lower states, for example,

$$P_{so}(J'') = Q_{21}(J'') - R_2(J'' - 1) \quad [1a]$$

$$Q_{so}(J'') = R_1(J'') - R_{12}(J'') \quad [1b]$$

$$R_{so}(J'') = R_{21}(J'') - Q_2(J'' + 1). \quad [1c]$$

These differences correspond to rotational fine-structure transitions in the $\tilde{X}^2\Pi$ state between levels of the same parity, where P_{so} , Q_{so} , and R_{so} are for $\Delta J = -1, 0, +1$, respectively. The experimental wavenumbers were taken from papers by Kakimoto and Kasuya (3) for the (000) $\tilde{X}^2\Pi_r$ state and from Kawaguchi *et al.* (7) for the (010) $^2\Delta_r$ and (020) $^2\Phi_r$ vibronic states. A similar calculation was done, using band origins determined by Merer and Travis (1) combined with band origins determined by Kohguchi *et al.* (15), to obtain the vibronic transition frequencies. A fit of these same vibronic transition frequencies was also carried out by Kohguchi *et al.* (15), using formulas derived from perturbation theory.

EXPERIMENTAL DETAILS

The far-infrared laser magnetic resonance spectrometer used for this work has been described in detail elsewhere (19). Two changes were recently made which improve the sensitivity and short-wavelength performance of the spectrometer (20). The

first is that the Zeeman-modulation frequency was increased from 13 to 40 kHz, with a proportionate increase in sensitivity. The second is that the diameter of the tube, which comprises the pump region of the LMR spectrometer, was reduced from 50.4 to 19 mm. Reduction of the diameter of the tube increases the overlap of the FIR radiation field at short wavelengths with the pumped lasing gas. This increases both the power of FIR laser lines below 100 μm and the number of lines lasing at these shorter wavelengths. These improvements have proven particularly important for the present experiment because all the vibronic transitions observed for CCN are at wavelengths well below 100 μm . The signals were detected with a gallium–germanium photoconductor, processed by a lock-in amplifier at f , and recorded with an xy plotter as a function of flux density. Since f detection using magnetic modulation was employed, the first derivative of the absorption profile was observed.

The CCN radical was produced using the method of hydrogen extraction by atomic fluorine, which has been proven effective in previous investigations (21). The fluorine atoms were generated by flowing 10% F_2 in He through a microwave discharge. Acetonitrile (CH_3CN) and helium were added downstream, where the fluorine atoms removed the hydrogen atoms, resulting in the production of CCN. A pale purple flame was observed when the production of CCN was optimized. The helium introduced with the acetonitrile acted primarily as a carrier gas and pushed the reaction zone down into the laser beam, generating larger signals. The partial pressures of the gases at which optimal signals were obtained were 53 Pa (400 mTorr) 10% F_2 in He, 4 Pa (30 mTorr) acetonitrile, and 53 Pa (400 mTorr) He. Two checks were performed on most of the transitions to confirm that the signals were due to CCN. Acetonitrile was replaced by either deuterated acetonitrile or methane. These checks eliminate species that contain hydrogen or nitrogen, respectively. In addition to these two tests, a third was performed on only a few lines. A horseshoe-shaped microwave discharge of length $n\lambda/4$ was used to discharge acetonitrile on its own. This check eliminated the possibility of a species that might contain fluorine. The signals obtained with this method were about the same intensity; however, it proved much more difficult to observe spectra at high-magnetic field because the discharge tended to become unstable as the magnetic field pinched it down.

Figure 1 shows a 0.2-T-wide scan of the $^R Q_{21}(39/2)$ transition and is a typical spectrum observed for CCN. A simulated spectrum of the same region calculated using the parameters determined in this work is included for comparison. The spectra were taken in both parallel ($E_\omega \parallel B_0$) and perpendicular ($E_\omega \perp B_0$) polarizations. Measurement scans were typically ≤ 0.02 T in width and the resonances were recorded by tuning the magnet to the center of the line and waiting several time constants (100 ms) for the magnetic field to stabilize. The magnet was calibrated periodically with an NMR gaussmeter. The overall experimental uncertainty is estimated to be $[(\pm 1 \times 10^{-4}) \times B(\text{T})]$ above 0.1 T and $\pm 1 \times 10^{-5}$ T below

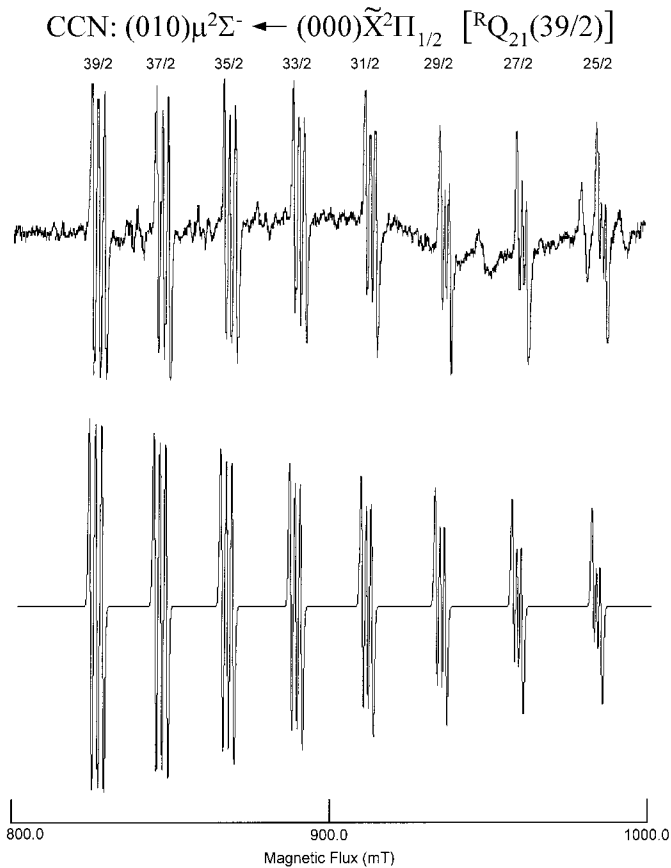


FIG. 1. Far-infrared laser magnetic spectrum (upper trace) and simulated spectrum (lower trace) of the $(010) \mu^2\Sigma^- \leftarrow (000) \tilde{X}^2\Pi_{1/2} [{}^R Q_{21}(39/2)]$ transition of CCN recorded in parallel polarization ($\Delta M_J = 0$). The spectrum was recorded using the $47.660\text{-}\mu\text{m}$ ($209.819231\text{ cm}^{-1}$) laser line of CH_3OD pumped by the $9R(8)$ line of CO_2 and covers a magnetic field range of 200 mT. The triplet splitting is due to the spin, $I = 1$, of the ${}^{14}\text{N}$ nucleus.

0.1 T, where B is the magnetic flux density. The laser frequency is accurate to $[2^{1/2} \times (2 \times 10^{-7}) \times \nu_{\text{laser}}]$.

RESULTS AND ANALYSIS

Thirteen FIR laser lines were used to record the LMR spectra reported in this paper. The details of these laser lines and the transitions recorded using each line are listed in Table 1. A total of 769 resonances were recorded and assigned, corresponding to 45 vibronic transitions and ranging in J'' from $1/2$ to $39/2$. The measurements were recorded over a frequency range of $192.3\text{--}209.8\text{ cm}^{-1}$ and $157.8\text{--}166.4\text{ cm}^{-1}$ for the $(010) \mu^2\Sigma^- \leftarrow (000) \tilde{X}^2\Pi_{1/2}$ and the $(010) \mu^2\Sigma^- \leftarrow (000) \tilde{X}^2\Pi_{3/2}$ transitions, respectively. Twenty-seven of the 45 transitions originated in the $\tilde{X}^2\Pi_{1/2}$ spin-orbit component and the remaining 18 originated in the $\tilde{X}^2\Pi_{3/2}$ spin-orbit component. Hyperfine structure was resolved in 103 of the 563 M_J components. All 12 types of transitions for a ${}^2\Sigma \leftarrow {}^2\Pi$ type

transition $P_1, Q_1, R_1, {}^o P_{21}, {}^R Q_{21}, {}^S R_{21}, P_2, Q_2, R_2, {}^o P_{12}, {}^P Q_{12}, {}^o R_{12}$ (22) were observed.

After initial experimental searches for CCN resonances, it was decided that predictions, which were more reliable, were needed in order to make correct assignments. With this in mind, a refit of the microwave data, reported by Ohshima and Endo (14) using our effective Renner-Teller Hamiltonian was necessary to verify the rotational, hyperfine structure, and lambda-doubling parameters for the ground state; details of the Hamiltonian are given later. In addition, we decided to perform a fit similar to that carried out by Kohguchi *et al.* (15) on the vibronic structure of the $(0\nu_2 0)$ manifold. However, they used expressions derived from perturbation theory, whereas we treated the same data with the N^2 Renner-Teller Hamiltonian. The vibronic-level separations used by Kohguchi *et al.* (15) were determined by a combination of their measurements and measurements by Merer and Travis (1). Kohguchi *et al.* recorded the ν_2 progression bands $(010) \Pi \leftarrow (000) \Pi_{1/2}$ and $(020) \Sigma, \Delta \leftarrow (000) \Pi_{1/2}$ in the $C-X$ transition. Merer and Travis measured the hot bands $(010) \Pi \leftarrow (010) \mu^2\Sigma^-, \Delta_{3/2,5/2}$, and $(020) \Delta \leftarrow (020) \Phi_{5/2,7/2}$. By taking the difference of the various band origins having the upper state in common, one determines the separation of the $(010) \mu^2\Sigma^- \leftarrow (000) {}^2\Pi$, $(010) {}^2\Delta \leftarrow (000) {}^2\Pi$, and $(020) {}^2\Phi \leftarrow (000) {}^2\Pi$ levels in the ground state. Merer and Travis also reported a value of 113.55 cm^{-1} for the separation of the $(010) {}^2\Delta \leftarrow (010) \mu^2\Sigma^-$ levels. In our fit of the vibronic levels, we corrected vibronic transition frequency for spin-orbit and rotational energies using the expression

$$\nu = \nu_0 - \frac{1}{2} A'_{\text{eff}} + B'z - \frac{1}{2} A''_{\text{eff}} + B''z, \quad [2]$$

where ν_0 is the vibronic level separation, A'_{eff} and A''_{eff} are the spin-orbit parameters, B' and B'' are the rotational constants for the upper and lower states, respectively, and $z = (J + 1/2)^2 - 1$. An energy level diagram of the vibronic levels can be seen in Fig. 2. These values were used to determine initial values for the vibrational, Renner-Teller, and true spin-orbit parameters $\omega_2, x_{22}, \epsilon\omega_2, A_{(000)}^{\text{true}}$, and $A_{(010)}^{\text{true}}$ while constraining the K -dependent correction term g_K at 2.5 cm^{-1} and B'' at the value determined from the microwave data. With the two types of data (microwave and vibronic levels) combined, a reasonable set of parameters was determined and a prediction that led to the assignment of several resonances was made. Once some assignments had been made and included in the fit, the remaining data could be assigned and further unobserved resonances predicted.

An effective Hamiltonian that describes the energy levels of a linear triatomic molecule in a ${}^2\Pi$ state and includes the Renner-Teller interaction explicitly was used to analyze the data obtained in this work. It is expressed in the N^2 formulation as the sum of several terms (23–26):

TABLE 1
FIR Laser Lines Used to Record LMR Spectra of the (010) $\mu^2\Sigma^- \leftarrow (000) \tilde{X}^2\Pi$ Transition of CCN

CO ₂ Pump Line ^a	FIR laser gas	Frequency (MHz)	Wavenumbers (cm ⁻¹)	Wavelength (μm)	Observed CCN transitions
(010)$\mu^2\Sigma^- \leftarrow (000) \tilde{X}^2\Pi_{1/2}$					
9R(8)	CH ₃ OD	6 290 222.3 ^b	209.819 231	47.660	^R Q ₂₁ (39/2), ^R R ₁ (35/2), ^R R ₁ (37/2), ^S R ₂₁ (15/2)
9R(6)	CD ₃ OH	6 153 279.0 ^b	205.251 294	48.721	^R Q ₂₁ (23/2), ^R Q ₂₁ (25/2), ^R R ₁ (21/2), ^R R ₁ (23/2)
9P(12)	¹³ CH ₃ OH	6 061 914.8 ^b	202.203 713	49.455	^R Q ₂₁ (13/2), ^R Q ₂₁ (15/2), ^R R ₁ (9/2), ^R R ₁ (11/2), ^S R ₂₁ (3/2)
10R(52)	CH ₃ OH	6 032 811.3 ^b	201.232 924	49.694	^R Q ₂₁ (9/2), ^R Q ₂₁ (11/2), ^R R ₁ (5/2), ^R R ₁ (7/2), ^S R ₂₁ (1/2)
10R(24)	CD ₃ OH	5 999 028.8 ^b	200.106 061	49.974	^R Q ₂₁ (3/2), ^R Q ₂₁ (5/2), ^R R ₁ (1/2)
10R(20)	CD ₃ OH	5 921 370.4 ^b	197.515 656	50.628	^Q P ₂₁ (5/2), ^Q P ₂₁ (7/2), ^Q P ₂₁ (9/2), ^Q Q ₁ (9/2), ^Q Q ₁ (11/2), ^Q Q ₁ (13/2), ^Q Q ₁ (15/2),
10R(46)	CH ₃ OH	5 764 826.7 ^b	192.293 920	52.004	^P P ₁ (13/2)
(010)$\mu^2\Sigma^- \leftarrow (000) \tilde{X}^2\Pi_{3/2}$					
9R(34)	CD ₃ OH	4 988 091.2 ^b	166.384 812	60.102	^R R ₂ (9/2)
9R(18)	CH ₃ OH	4 865 709.8 ^a	162.302 609	61.613	^Q Q ₂ (13/2), ^Q Q ₂ (15/2), ^R R ₂ (3/2), ^Q R ₁₂ (9/2), ^Q R ₁₂ (11/2)
10R(18)	¹³ CH ₃ OH	4 762 125.4 ^b	158.847 405	62.954	^P P ₂ (3/2), ^Q P ₁₂ (3/2), ^P Q ₁₂ (3/2), ^P Q ₁₂ (5/2), ^P Q ₁₂ (7/2)
10R(16)	CH ₃ OH	4 761 182.4 ^a	158.815 950	62.966	^P P ₂ (3/2), ^Q P ₁₂ (3/2), ^P Q ₁₂ (3/2), ^P Q ₁₂ (5/2), ^P Q ₁₂ (7/2), ^P Q ₁₂ (9/2)
9P(12)	¹³ CH ₃ OH	4 751 340.9 ^a	158.487 673	63.096	^P Q ₁₂ (7/2)
9P(34)	CH ₃ OH	4 730 860.6 ^a	157.804 524	63.370	^P P ₂ (5/2), ^P P ₂ (7/2), ^P P ₂ (9/2), ^Q P ₁₂ (3/2), ^Q P ₁₂ (5/2), ^P Q ₁₂ (9/2), ^P Q ₁₂ (11/2), ^P Q ₁₂ (13/2)

^a N. G. Douglas, Millimeter and Sub-millimeter Wavelength Lasers, Springer Series in Optical Sciences, Vol. 61.

^b New FIR laser line, frequency measured in our laboratory. The accuracy of the measured laser frequencies is 2×10^{-7} xv.

$$\mathbf{H}_{\text{eff}} = \mathbf{H}_{\text{vib}} + \mathbf{H}_{\text{RT}} + \mathbf{H}_{\text{rot}} + \mathbf{H}_{\text{so}} + \mathbf{H}_{\text{sr}} + \mathbf{H}_{\text{Adoub}} + \mathbf{H}_{\text{Idoub}} + \mathbf{H}_{\text{mhfs}} + \mathbf{H}_{\text{Q}} + \mathbf{H}_{\text{Zeem}}. \quad [3]$$

The form of each individual term is now dealt with in turn. The vibrational Hamiltonian, \mathbf{H}_{vib} , is used to generate a set of basis states for the two-dimensional oscillator (the bending vibration),

$$\mathbf{H}_{\text{vib}}/hc|v_2l\rangle = [(v_2 + 1)\omega_2 + (v_2 + 1)x_{22} + g_{22}l^2]|v_2l\rangle, \quad [4]$$

where $|v_2l\rangle$ is the eigenfunction of the harmonic oscillator. The Renner–Teller Hamiltonian is written

$$\mathbf{H}_{\text{RT}}/hc = 1/2\epsilon\omega_2[q_+^2e^{-2i\theta} + q_-^2e^{+2i\theta}] + 1/4(\epsilon\omega_2)_D[(q_+^2e^{-2i\theta} + q_-^2e^{+2i\theta}), \mathbf{N}^2]_{++}, \quad [5]$$

where q_{\pm} is the dimensionless vibrational ladder operator and θ is the electronic azimuthal angle. The second term in this expression describes the rotational distortion of the Renner–

Teller Hamiltonian, see (24). The next term in Eq. [3] represents the rotational kinetic energy of the nuclei

$$\mathbf{H}_{\text{rot}} = B\mathbf{N}^2 - D\mathbf{N}^2 \cdot \mathbf{N}^2 \quad [6]$$

in its usual \mathbf{N}^2 form, where $\mathbf{N} = \mathbf{J} + \mathbf{S}$, again with centrifugal distortion effects. The spin–orbit coupling term is also well known,

$$\mathbf{H}_{\text{so}} = AL_zS_z + 1/2A_D[L_zS_z, \mathbf{N}^2]_{++}. \quad [7]$$

The spin–rotation interaction can be described by

$$\mathbf{H}_{\text{sr}} = \gamma\mathbf{N} \cdot \mathbf{S} + \gamma_D(\mathbf{N} \cdot \mathbf{S})\mathbf{N}^2 + \gamma_GN_zS_z; \quad [8]$$

the third term on the right-hand side is slightly novel (27). It describes the vibronic coupling with the $^2\Sigma$ and $^2\Delta$ states of the molecule. The lambda-type doubling Hamiltonian for a molecule in a $^2\Pi$ state is written

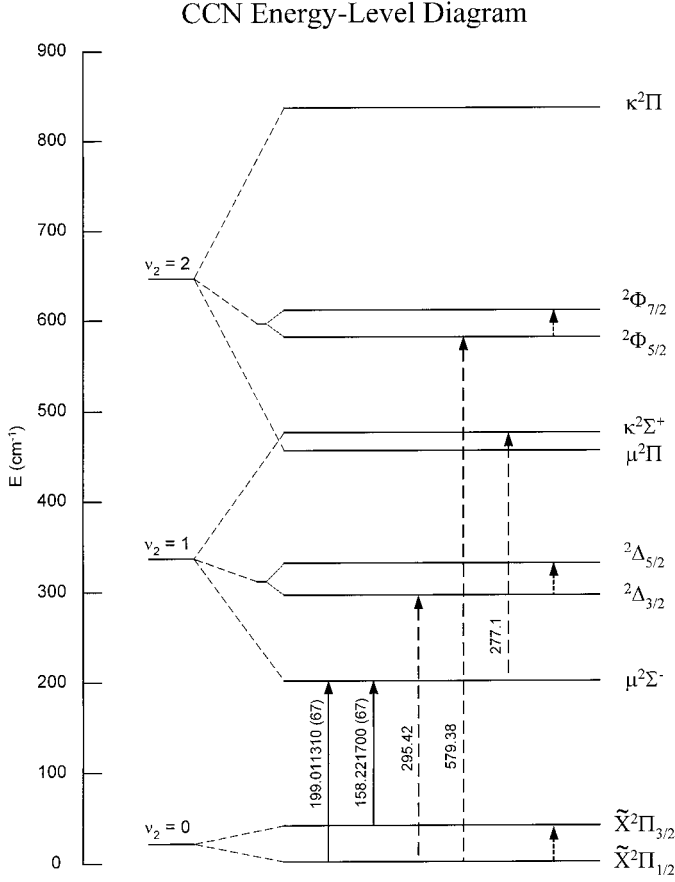


FIG. 2. Energy-level diagram of the $(0, \nu_2, 0)$ vibronic levels. The transitions observed in this work are shown by solid lines. The wavenumber labels associated with these transitions are the calculated band origins from our parameters. The transitions represented as dashed lines are the additional transitions included in the fit. The wavenumber labels are the values used in the fit (they are left off the spin-orbit transitions because there are multiple values for these transitions, see Table 4).

$$\begin{aligned}
 \mathbf{H}_{\Lambda\text{doub}} = & 1/2p(N_+S_+e^{-2i\theta} + N_-S_-e^{+2i\theta}) \\
 & - 1/2q(N_+^2e^{-2i\theta} + N_-^2e^{+2i\theta}) \\
 & + 1/4(p_D + 2q_D) \\
 & \times [(N_+S_+e^{-2i\theta} + N_-S_-e^{+2i\theta}), \mathbf{N}^2]_+ \\
 & - 1/4q_D[(N_+^2e^{-2i\theta} + N_-^2e^{+2i\theta}), \mathbf{N}^2]_+,
 \end{aligned} \tag{9}$$

where the ladder operators N_+ and S_+ have their usual meanings. The l -type doubling term $\mathbf{H}_{\text{ldoub}}$ is cast in a similar form,

$$\begin{aligned}
 \mathbf{H}_{\text{ldoub}} = & 1/2p_G(N_+S_+e^{-2i\phi} + N_-S_-e^{+2i\phi}) \\
 & - 1/2q_G(N_+^2e^{-2i\phi} + N_-^2e^{+2i\phi}),
 \end{aligned} \tag{10}$$

except that here ϕ is the bending vibration azimuthal angle. The operator \mathbf{H}_{mhfs} represents the magnetic hyperfine interactions, which are, following Frosch and Foley (28),

$$\begin{aligned}
 \mathbf{H}_{\text{mhfs}} = & aI_zL_z + b\mathbf{I} \cdot \mathbf{S} + cI_zS_z \\
 & + 1/2d(I_+S_+e^{-2i\theta} + I_-S_-e^{+2i\theta}).
 \end{aligned} \tag{11}$$

In this formulation, the parameter c relates to the dipole-dipole coupling term and b is related to the Fermi-contact parameter b_F by $b_F = b + c/3$. The electric-quadrupole interaction for the ^{14}N -nucleus is described by

$$\mathbf{H}_Q = -eT^2(\mathbf{Q}) \cdot T^2(\nabla\mathbf{E}). \tag{12}$$

For a $^2\Pi$ state, there are two determinable parameters

$$eQq_0 = -2eQ\langle\Lambda = 1|T_0^2(\nabla\mathbf{E})|\Lambda = 1\rangle \tag{13}$$

and

$$eQq_2 = -2\sqrt{6}eQ\langle\Lambda = \pm 1|T_{\pm 2}^2(\nabla\mathbf{E})|\Lambda = \mp 1\rangle. \tag{14}$$

Finally, we deal with the effects of the external magnetic field, described by the Zeeman Hamiltonian \mathbf{H}_{Zeem} ,

$$\begin{aligned}
 \mathbf{H}_{\text{Zeem}} = & g_L\mu_B B_0 L_Z + g_S\mu_B B_0 S_Z + g_I\mu_B(B_X S_X + B_Y S_Y) \\
 & - g_r\mu_B B_0 N_Z - g_r'\mu_B(N_+B_+e^{-2i\theta} + N_-B_-e^{2i\theta}) \\
 & + g_r'\mu_B(S_+B_+e^{-2i\theta} + S_-B_-e^{2i\theta}) - g_N\mu_N I_Z B_0,
 \end{aligned} \tag{15}$$

where the first two terms describe the dominant contributions from the electron orbital and spin angular momenta and the remaining three terms represent the smaller contributions, described in Ref. (26).

The matrix representation of this effective Hamiltonian was constructed in a Hund's case (a), parity-conserving basis set,

$$\begin{aligned}
 |\Lambda\nu_2lS; J\pm\rangle = & 2^{-1/2}\{|\eta\Lambda; \nu_2l; S\Sigma; JPM\rangle \\
 & \pm (-1)^{J-S-l+s}|\eta - \Lambda; \nu_2 - l; S - \Sigma; J - PM\rangle\},
 \end{aligned} \tag{16}$$

where $K = \Lambda + l$, $P = K + \Sigma$, and s is odd for a Σ^- electronic state and even for all other electronic states. The choices of upper and lower sign correspond to states of $+$ and $-$ parity, respectively. We note that there is a phase choice implicit in the basis function in Eq. [16] so that, for the operator terms in \mathbf{H}_{eff} which are parity dependent,

$$\langle\Lambda = \pm 1|e^{\pm 2i\theta}|\Lambda = \mp 1\rangle = -1 \tag{17a}$$

and

$$\langle l = \pm 1|e^{\pm 2i\phi}|l = \mp 1\rangle = +1. \tag{17b}$$

TABLE 3
Details of the Microwave Data Included
in the Least-Squares Fit^a

$J \leftarrow J'$	$F' \leftarrow F''$	Parity	Frequency (MHz)	o. - c. (kHz)
3/2 \leftarrow 1/2	5/2 \leftarrow 3/2	- \leftarrow +	35 422.683 7	-0.4
	3/2 \leftarrow 1/2	- \leftarrow +	35 429.396 8	-0.6
	3/2 \leftarrow 3/2	- \leftarrow +	35 440.232 5	0.8
	1/2 \leftarrow 1/2	- \leftarrow +	35 442.943 9	1.0
	1/2 \leftarrow 3/2	- \leftarrow +	35 453.776 4	-0.8
	3/2 \leftarrow 3/2	+ \leftarrow -	35 427.931 7	0.1
	5/2 \leftarrow 3/2	+ \leftarrow -	35 472.588 7	0.5
	1/2 \leftarrow 1/2	+ \leftarrow -	35 486.586 6	-0.1
	3/2 \leftarrow 1/2	+ \leftarrow -	35 510.659 9	-0.3
	1/2 \leftarrow 3/2	+ \leftarrow -	35 403.858 0	-0.1

^aData taken from Ref. (14), o. - c. determined in this work.

The effective Hamiltonian was used to analyze the data listed in Tables 2, 3, 4, and 5. Table 2 (available as supplementary data) reports the details of the FIR LMR data from this work. Table 3 lists the 10 transitions, reported in the microwave study of CCN in the $\tilde{X}^2\Pi_{1/2}$ component by Ohshima and Endo (14), that were included in the fit. Table 4 gives the details of the 55 spin-orbit transitions calculated as combination differences from electronic transitions reported in Refs. (3) and (7). Table 5 shows the five vibronic transitions, four of which were calculated as stated above, and the (010) $\kappa^2\Sigma^+ \leftarrow$ (010) $\mu^2\Sigma^-$ separation was estimated from the Q -branch bandheads reported by Hakuta and Uehara (4). The modification to the Hamiltonian extended the matrix representation to span states of the same vibronic symmetry off-diagonal by $\Delta\nu_2 = \pm 2, \pm 4, \dots$, for each basis state $|\nu_1, \nu_2, \nu_3; \Lambda IK; S\Sigma; JPM_J; \pm\rangle$. This allowed the matrix elements of the Renner-Teller effective Hamiltonian (23) to be included explicitly and the total representation to be diagonalized. To model the Zeeman effect accurately, the matrix representation also spanned elements off-diagonal in J by $\Delta J = \pm 1$, that is, between states of the same M_J in neighboring rotational levels. A basis set truncated at $\Delta\nu_2 = \pm 6$ and $\Delta J = \pm 4$ was found to be adequate for the present analysis. The effects of the Fermi-type resonance between the bending and the stretching vibrational levels of CCN were not included in our analysis because none of the states involved in this work are directly affected by such resonances.

Each observed resonance listed in Table 2 was initially given a weight equal to the inverse square of the estimated experimental uncertainty. The estimated experimental uncertainty of the FIR LMR data was determined to be 2 MHz, based on the accuracy of the laser frequency, the uncertainty in the measurement of the magnetic flux, and typical tuning rates for the CCN transitions. The microwave data, spin-orbit data, and vibronic data were given experimental uncertainties of 1 kHz, 150 MHz (0.005 cm^{-1}), and 1.5 GHz (0.05 cm^{-1}), respectively. After several attempted fits, 4 of the 769 resonances had

residuals much greater than three times their uncertainty and, after reinvestigating the spectra, they were subsequently given zero weight. The (010) $\kappa^2\Sigma^+ \leftarrow$ (010) $\mu^2\Sigma^-$ vibronic transition was also given zero weight because the uncertainty was too large to include that data point in the fit.

The data set including all four types of data required 32 parameters, 30 varied and 2 (g_K and g_N) fixed, to model the data. The parameters determined in this fit are listed in Table 6 both in units of megahertz and reciprocal centimeters. The best previously obtained values, where available, are also included in Table 6 for comparison. The parameters determined include vibrational and Renner-Teller parameters ω_2 , $\epsilon\omega_2$, x_{22} , and g_K , spin-orbit and rotational parameters $A_{(000)}^{\text{true}}$, $A_{(010)}^{\text{true}}$, $B_{(000)}$, $B_{(010)}$, $D_{(000)}$, $D_{(010)}$, $\gamma_{(000)}$, $\gamma_{(010)}$, $\gamma_{D(010)}$, and $\epsilon\omega_{2D}$ (24), lambda-type doubling parameters ($p + 2q$), q , and ($p_D + 2q_D$), hyperfine parameters a , b , ($b + c$), d , eQq_0 , and eQq_2 , and Zeeman parameters g_S , g_L , Δg_L , g_r , g_l , g_r' , and ($g_l' - g_r'$). The parameter g_K was fixed at 2.5 cm^{-1} , the value obtained by Brazier *et al.* (5), while g_N was fixed to the nuclear magnetic moment for ^{14}N (0.40376 nuclear magnetons) (29). Table 7 lists a range of zero-field transition frequencies, calculated using the constants determined in this work. The transitions observed in this work are marked and should be determined more reliably than those that were not observed.

DISCUSSION

We detected transitions in the ν_2 fundamental band of the CCN radical by far-infrared LMR. The upper level of this transition is pushed to significantly lower energies by the Renner-Teller effect in this molecule (see Fig. 2). This is only the third example of the detection of a low-frequency bending vibration in the far-infrared region. The first was for C_3 (30), and the second was for FeD_2 (31). It is interesting to note that observations have been made in this case over a wide range of J values; observations by LMR are usually restricted to the lowest J values because the magnetic moment falls off quadratically with J . The reason for the extensive observations in the case of CCN is that the transition takes place between levels that conform to Hund's case (a) coupling (lower state) and levels which are Hund's case (b) (upper state).

Several advances in the understanding of the energy levels of the CCN radical were made in this study. First, this is the most detailed analysis of the vibronic energy levels in the $\tilde{X}^2\Pi$, state of CCN to date. Thirty parameters were determined in the analysis and many of them improved upon the old values by roughly an order of magnitude. In addition, seven of the 30 parameters determined in the fit had not been determined before. A full set of nuclear g -factors and nuclear hyperfine parameters were determined for the first time for CCN.

The band origins of the $2_0^1, \mu^2\Sigma^- \leftarrow ^2\Pi$ transition studied in this work depend on several parameters in the effective Hamiltonian, primarily ω_2 , $\epsilon\omega_2$, x_{22} , g_K , and A . We therefore included the vibrational intervals, listed in Table 5, in our fit in

TABLE 4
Details of the Spin–Orbit Data Included in the Least-Squares Fit

Vibronic level	Transition	Frequency (cm ⁻¹)	o. – c. (cm ⁻¹)	Frequency (MHz)	o. – c. (MHz)
(000) $\tilde{X}^2\Pi_r$	P _{so} (7/2)	36.887 9	0.0003	1 105 870	8.982
	P _{so} (13/2)	34.740 0	0.0002	1 041 480	5.390
	P _{so} (15/2)	34.062 6	0.0069	1 021 170	207.414
	P _{so} (17/2)	33.385 8	-0.0015	1 000 880	-45.535
	P _{so} (19/2)	32.736 7	0.0024	981 421	72.370
	P _{so} (21/2)	32.100 9	0.0042	962 360	125.317
	P _{so} (23/2)	31.475 5	0.0012	943 611	34.706
	Q _{so} (3/2)	39.601 4	-0.0051	1 187 220	-152.337
	Q _{so} (5/2)	39.649 8	0.0029	1 188 670	86.732
	Q _{so} (7/2)	39.706 8	0.0036	1 190 380	106.974
	Q _{so} (9/2)	39.784 9	0.0088	1 192 720	264.253
	Q _{so} (11/2)	39.860 9	-0.0035	1 195 000	-104.277
	Q _{so} (13/2)	39.972 0	0.0032	1 198 330	95.883
	Q _{so} (15/2)	40.094 1	0.0053	1 201 990	158.029
	Q _{so} (17/2)	40.221 2	-0.0033	1 205 800	-99.386
	Q _{so} (19/2)	40.372 3	-0.0031	1 210 330	-92.936
	Q _{so} (21/2)	40.539 7	-0.0019	1 215 350	-57.158
	R _{so} (5/2)	42.462 7	0.0000	1 273 000	-1.148
	R _{so} (7/2)	43.330 3	0.0066	1 299 010	198.163
	R _{so} (9/2)	44.201 9	0.0014	1 325 140	42.004
	R _{so} (15/2)	46.928 1	0.0023	1 406 870	68.203
	R _{so} (17/2)	47.871 5	0.0061	1 435 150	181.999
	R _{so} (19/2)	48.819 4	-0.0006	1 463 570	-17.590
(010) $^2\Delta_r$	P _{so} (13/2)	29.541 5	-0.0018	885 631	-52.609
	P _{so} (15/2)	28.871 2	-0.0018	865 536	-54.355
	P _{so} (17/2)	28.223 0	0.0019	846 104	56.838
	P _{so} (19/2)	27.587 4	0.0001	827 049	3.163
	P _{so} (23/2)	26.376 2	0.0033	790 738	98.269
	P _{so} (25/2)	25.799 6	0.0078	773 452	234.425
	Q _{so} (5/2)	34.444 8	0.0027	1 032 630	81.023
	Q _{so} (9/2)	34.593 3	-0.0016	1 037 080	-46.849
	Q _{so} (11/2)	34.692 3	-0.0068	1 040 050	-204.505
	Q _{so} (13/2)	34.821 1	-0.0015	1 043 910	-44.277
	Q _{so} (15/2)	34.970 2	0.0062	1 048 380	185.043
Q _{so} (17/2)	35.125 0	0.0011	1 053 020	31.601	
Q _{so} (19/2)	35.298 1	-0.0032	1 058 210	-95.307	
Q _{so} (21/2)	35.491 9	-0.0049	1 064 020	-145.446	

order to separate these parameters. In addition, the spin–orbit data in Table 4 provided much needed information about the spin splitting in the $\nu_2 = 1$ and 2 levels. The spin–orbit splitting in the zero-point level is accurately determined from the differences between the two sets of data recorded around 50 and 61 μm in the present study. The inclusion of these additional data allows a more reliable set of parameters to be

determined. However, even with their involvement, these vibronic parameters are highly correlated and we chose, in the end, to constrain the parameter g_k to the value of 2.5 cm⁻¹ determined by Brazier *et al.* (5). If this parameter was allowed to vary in the fit, it was barely determinable, and the standard deviations of ω_2 , $\epsilon\omega_2$, and x_{22} increased considerably so that x_{22} was not well determined either. This is understandable

TABLE 4—Continued

Vibronic level	Transition	Frequency (cm ⁻¹)	o. – c. (cm ⁻¹)	Frequency (MHz)	o. – c. (MHz)
(020) ² Φ _r	Q _{so} (23/2)	35.705 0	-0.0043	1 070 410	-127.906
	Q _{so} (25/2)	35.937 5	-0.0015	1 077 380	-45.210
	R _{so} (5/2)	37.287 1	0.0019	1 117 840	58.280
	R _{so} (7/2)	38.165 1	0.0009	1 144 160	27.091
	R _{so} (9/2)	39.056 4	-0.0056	1 170 880	-166.303
	R _{so} (11/2)	39.972 7	-0.0058	1 198 350	-172.189
	R _{so} (13/2)	40.910 6	-0.0027	1 226 470	-80.688
	R _{so} (17/2)	42.835 6	-0.0020	1 284 180	-60.874
	R _{so} (19/2)	43.820 3	-0.0064	1 313 700	-191.979
	R _{so} (21/2)	44.831 7	-0.0013	1 344 020	-38.852
	P _{so} (19/2)	21.763 1	-0.0032	652 441	-94.749
	P _{so} (21/2)	21.190 1	0.0059	635 263	176.723
	P _{so} (23/2)	20.624 4	0.0015	618 303	45.284
	Q _{so} (21/2)	29.803 1	0.0047	893 474	141.670
	Q _{so} (23/2)	30.062 2	0.0062	901 242	184.842
	R _{so} (17/2)	37.139 0	-0.0006	1 113 400	-19.085
	R _{so} (21/2)	39.229 1	-0.0023	1 176 060	-69.529
	R _{so} (23/2)	40.311 2	0.0034	1 208 500	101.923

because we have only four different vibronic transitions included in the data and none of them involves the (010) $\kappa^2\Sigma^+$ vibronic level. It is essential to have information on all three vibronic components of the $\nu_2 = 1$ vibrational level in order to determine the Renner parameter to a high degree of accuracy. Of course, a value for g_K can be determined if the parameter x_{22} is held fixed. However, such a value depends directly on the assumed value for x_{22} , and we have a slightly better knowledge of g_K than of x_{22} from other work. If g_K is constrained to zero in the fit, the standard deviation of the spin-orbit data in Table 4 increases by a factor of about 3 while the other types of data are hardly affected by this change.

An important difference in our fit compared with those of previous workers is that we included the effects of the Renner–Teller coupling explicitly in our Hamiltonian, rather than treating the effects by matrix elements off-diagonal in ν_2 by second-order perturbation theory. With such an approach, we are

able to model the energy levels of CCN much more reliably because the Renner–Teller parameter for this molecule is quite large ($\epsilon = 0.4179$). Indeed the failure of the perturbation-theory approach can be gauged from the discrepancy between the value for $\epsilon\omega_2$ determined in this work (133.639 cm⁻¹) and that determined previously (137.7 cm⁻¹) by Kohguchi *et al.* (15). Again, reference to Table 6 shows that the “true” spin-orbit coupling constant has only a weak dependence on ν_2 . When the effects of the $\Delta\nu_2 = 2$ Renner–Teller matrix elements are taken into account, the spin-orbit splitting, A^{eff} , becomes markedly smaller. For the unique level, second-order perturbation theory gives

$$A^{\text{eff}} = A^{\text{true}}[1 - \epsilon^2 K(K + 1)/8]. \quad [18]$$

We can use this formula to estimate the effective spin-orbit

TABLE 5
Details of the Bending Vibronic Intervals Included in the Least-Squares Fit

Transition	Parity	Frequency (cm ⁻¹)	o. – c. (cm ⁻¹)	Frequency (MHz)	o. – c. (MHz)	Uncertainty (cm ⁻¹)
(010) $\mu^2\Sigma^- \leftarrow (000) \tilde{X}^2\Pi_{1/2}$ [Q(1/2)]	- ← +	199.06	0.049	5 967 700	1457.317	0.05
(010) $\mu^2\Sigma^- \leftarrow (000) \tilde{X}^2\Pi_{3/2}$ [P(3/2)]	- ← +	158.28	0.058	4 745 100	1747.837	0.05
(010) $\kappa^2\Sigma^+ \leftarrow (010) \mu^2\Sigma^-$ [Q(1/2)]	+ ← -	277.10	0.764	8 307 000	22850.195	0.00
(010) $^2\Delta \leftarrow (000) \tilde{X}^2\Pi_{1/2}$ [R(1/2)]		295.42	0.118	8 856 500	3533.784	0.05
(020) $^2\Phi \leftarrow (000) \tilde{X}^2\Pi_{1/2}$ [S(1/2)]		579.38	-0.069	17 369 000	-2057.183	0.05

TABLE 6
Molecular Parameters Determined in the Analysis of CCN^a

Parameter	This work (MHz)	This work (cm ⁻¹)	Previous work (cm ⁻¹)	Ref.
ω_2	9 586 716. (1338.)	319.778 (45)	319.9 (1.1)	(15)
$\varepsilon\omega_2$	4 006 388. (1241.)	133.639 (41)	137.7 (1.1) ^c	(15)
$(\varepsilon\omega_2)_D$	-16.60 (61)	-0.000 554 (20)	--	
g_K	75 000 ^b	2.5 ^b	2.5	(5)
x_{22}	12 948. (437.)	0.432 (15)	--	
$A_{(000)}^{\text{true}}$	1 275 299. (38.)	42.539 4 (13)	42.327 9 (32)	(13)
$B_{(000)}$	11 933.790 (45)	0.398 068 4 (15)	0.398 228 292 7 (48)	(14)
$D_{(000)}$	0.007 34 (17)	0.245 1 (55) x 10 ⁻⁶	0.220 6 (46) x 10 ⁻⁶	(3)
$\gamma_{(000)}$	-70.5 (1.2)	-0.002 352 (41)	-0.003 757 (46)	(3)
$A_{(010)}^{\text{true}}$	1 262 228. (132.)	42.103 4 (44)	41.423 (45) ^d	(7)
$B_{(010)}$	12 018.62 (78)	0.400 898 (26)	0.401 819 (57) ^e	(7)
$D_{(010)}$	0.008 23 (16)	0.274 6 (55) x 10 ⁻⁶	0.148 (27) x 10 ⁻⁶ ^e	(7)
$\gamma_{(010)}$	-27.3 (1.2)	-0.000 913 (41)	0.007 56 (16) ^e	(7)
$\gamma_D(010)$	0.002 83 (25)	0.945 (84) x 10 ⁻⁷	-0.90 (28) x 10 ⁻⁷ ^e	(7)
$A_D(010)$	3.52 (47)	0.000 117 (16)	--	
$(p + 2q)$	44.579 1 (60)	0.001 487 00 (20)	0.001 49 (12) ^f	(3,14)
q	7.649 (71)	0.000 255 2 (24)	0.000 237 91 (88)	(3)
$(p_D + 2q_D)$	0.011 5 (16)	0.384 (53) x 10 ⁻⁶	--	
a	31.63 (39)	0.001 055 (13)	0.001 199 557 (25) ^g	(14)
b	19.435 (27)	0.000 648 31 (88)	0.000 658 9 (10)	(14)
$(b + c)$	-11.48 (74)	-0.000 382 (25)	--	
d	46.767 38 (53)	0.001 559 992 (18)	0.001 559 993 (22)	(14)
eQq_0	-4.822 1 (14)	-0.000 160 849 (47)	-0.000 160 85 (62)	(14)
eQq_2	9.208 (66)	0.000 307 1 (22)	-0.000 306 5 (29)	(14)
g_s		2.001 97 (12)	2.002 099	(13)
g_L		1.008 82 (52)	0.999 890	(13)
Δg_L		-0.019 02 (52)	-0.00772	(13)
g_r		-0.000 080 1 (64)	--	
g_I		0.001 17 (12)	--	
g_r^c		0.000 129 1 (85)	--	
$(g_I' - g_r^c)$		0.001 559 (29)	--	
g_N		0.403 76 ^b	--	

^a Numbers in parentheses are one standard deviation and apply to the last quoted digits.

^b Parameter constrained to this value in the fit (see text).

^c The value of $\varepsilon\omega_2$ was calculated from the reported values of ω_2 and ε .

^d Converted from the originally reported value of A^{eff} using the value of ε calculated in this work.

^e These values are specific to the (010) $\mu^2\Sigma^-$ vibronic state.

^f Calculated using the reported values of p and q .

^g Reported as $a - (b+c)/2$.

TABLE 7
Calculated Zero-Field Transition Frequencies, without Hyperfine, for the (010) $\mu^2\Sigma^- \leftarrow (000) \tilde{X}^2\Pi$
Transition of CCN (in MHz)

$\mu^2\Sigma^- \leftarrow \tilde{X}^2\Pi_{1/2}$						
J''	$P_1(J'')$	$Q_1(J'')$	$R_1(J'')$	$^O P_{21}(J'')$	$^R Q_{21}(J'')$	$^S R_{21}(J'')$
1/2		5966211.4	5990373.3 ^b		5990027.3	6038138.8 ^a
3/2	5930692.9	5954987.8	6003197.1	5954641.8	6002620.3 ^a	6074866.1 ^a
5/2	5895791.7	5944219.6	6016477.6 ^b	5943642.9 ^a	6015670.0 ^b	6112047.5
7/2	5861347.8	5933905.6	6030214.4 ^a	5933098.0 ^a	6029175.7	6149681.6
9/2	5827360.6	5924044.4 ^b	6044406.7 ^b	5923005.7 ^a	6043136.6 ^b	6187766.4
11/2	5793829.7	5914634.2 ^b	6059053.4 ^a	5913364.2	6057551.6 ^b	6226299.7
13/2	5760753.8 ^b	5905673.0 ^a	6074153.0	5904171.3	6072419.3 ^b	6265278.9
15/2	5728131.8	5897158.4 ^a	6089703.8	5895424.8	6087737.7 ^b	6304701.4 ^a
17/2	5695962.0	5889087.9	6105703.8	5887121.8	6103504.9	6344563.9
19/2	5664242.4	5881458.5	6122150.7	5879259.6	6119718.5	6384863.3
21/2	5632971.0	5874267.2	6139042.0 ^b	5871834.9	6136375.8	6425595.9
23/2	5602145.2	5867510.6	6156374.6 ^b	5864844.4	6153473.9 ^b	6466757.9
25/2	5571762.4	5861185.2	6174145.7	5858284.4	6171009.7 ^b	6508345.3

$\mu^2\Sigma^- \leftarrow \tilde{X}^2\Pi_{3/2}$						
J''	$P_2(J'')$	$Q_2(J'')$	$R_2(J'')$	$^O P_{12}(J'')$	$^P Q_{12}(J'')$	$^R R_{12}(J'')$
3/2	4767228.7 ^b	4815294.6	4887452.9 ^b	4743367.2 ^a	4767574.7 ^a	4815871.4
5/2	4754998.3 ^b	4827151.8	4923402.9	4707273.6 ^a	4755575.0 ^b	4827959.5
7/2	4742742.0 ^a	4838979.8	4959325.6	4671151.9	4743549.7 ^a	4840018.5
9/2	4730461.4 ^a	4850778.8	4995222.1 ^a	4635002.8	4731500.2 ^a	4852048.9 ^a
11/2	4718158.3	4862549.5	5031093.8	4598827.5	4719428.3 ^a	4864051.2 ^a
13/2	4705834.6	4874292.8 ^a	5066942.2	4562627.4	4707336.3 ^a	4876026.5
15/2	4693492.6	4886010.0 ^b	5102769.2	4526404.0	4695226.3	4887976.0
17/2	4681134.8	4897702.3	5138576.9	4490159.4	4683100.9	4899901.2
19/2	4668763.9	4909371.6	5174367.6	4453895.5	4670962.8	4911803.8
21/2	4656382.8	4921019.6	5210143.7	4417614.8	4658815.0	4923685.8
23/2	4643994.5	4932648.5	5245907.9	4381319.8	4646660.7	4935549.3
25/2	4631602.3	4944260.6	5281663.1	4345013.3	4634503.0	4947396.6

^a Transition observed in this work.

^b Transition observed in this work with hyperfine structure resolved in one or more resonances.

splitting in the two lowest bending levels of CCN and compare them with the corresponding quantities determined by a fit of the experimental data. The results are given in Table 8, where it can be seen that the second-order perturbation expressions significantly underestimate the size of the splitting.

In the present study, we were able to observe the ¹⁴N-nuclear hyperfine splitting for levels in the $^2\Pi_{3/2}$ spin component of

CCN for the first time. When combined with the microwave observations of the $^2\Pi_{1/2}$ component, it is now possible to make a complete determination of the hyperfine parameters for the (000) level of the ground electronic state of this molecule (see Table 6). The magnetic hyperfine parameters provide direct information on the distribution of the open-shell electrons in the ground state wavefunction (32). The values of the param-

TABLE 8
Values of the Spin-Orbit Splitting of the First Two Bending Vibrational Levels (in cm^{-1})

Vibronic level	A^{true}	$A^{\text{eff}(2) a}$	$A^{\text{eff}}(\text{exp.})$
$\nu_2 = 0$ $K = 1$	42.5394	40.6820	40.37990 ^b
$\nu_2 = 1$ $K = 2$	42.1034	36.5884	35.9977 ^c

^a Value estimated from second-order perturbation expression, Eq. [18].

^b Ref. (3).

^c Ref. (7).

TABLE 9
¹⁴N-Nuclear Hyperfine Parameters (in MHz) and Related Expectation Values (in m⁻³)
for CCN and Related Molecules

Parameter	CCN ^a	NO ^b	NCN ^c	NCO ^d	N ^e
<i>a</i>	31.63(39)	84.20378(76)		62.363(21)	
(<i>b+c</i>)	-11.48(74)			-16.97(42)	
<i>b</i>	19.435(27)			30.597(225)	
<i>d</i>	46.76738(53)	112.59718(13)		88.485(13)	
<i>c</i>	-30.915(746)	-58.8820(22)	-25.9	-47.57(23)	
<i>b_F</i>	9.130(25)	22.3792(29)	14.1	14.74(15)	
<i>eQq₀</i>	-4.8221(14)	-1.85671(26)		-2.211(12)	
<i>eQq₂</i>	9.208(66)	23.1147(83)		-16.16(51)	
10 ⁻³⁰ ⟨ <i>r</i> ⁻³ ⟩ _ℓ	5.541	14.751		10.925	20.21
10 ⁻²⁹ Ψ(0) ²	1.907	4.675	2.945	3.079	2.187
10 ⁻³⁰ ⟨(3cos ² θ-1)/ <i>r</i> ³ ⟩ _s	-3.607	-6.870	-3.022	-5.550	
10 ⁻³⁰ ⟨sin ² θ/ <i>r</i> ³ ⟩ _s	5.456	13.136		10.323	
10 ⁻³⁰ ⟨ <i>r</i> ⁻³ ⟩ _s	6.389	16.270		12.710	22.22

^a Ref. (14) and present work

^b Ref. (33)

^c Ref. (34)

^d Refs. (35,24)

^e Refs. (36,37)

eters and the electronic spatial expectation values derived from them are summarized in Table 9. For comparison, we give the corresponding hyperfine quantities for the related species, NO in its $\tilde{X}^2\Pi$ ground state (33), NCN in its $\tilde{X}^3\Sigma^-$ state (34), NCO in its $\tilde{X}^2\Pi$ state (24, 35), and atomic nitrogen (36, 37). None of these species is isoelectronic with CCN (hyperfine splitting was not observed for other 15-electron molecules), but the open-shell orbital is the same for the triatomic species. It is a nonbonding π_s orbital, which contains only one electron for CCN (1). If we represent this orbital as a linear combination of atomic $2p\pi$ orbitals on each of the three atoms, we can write

$$\Psi_\pi = c_1\phi_1 + c_2\phi_2 + c_3\phi_3. \quad [19]$$

For a symmetrical AB_2 molecule, c_2 equals zero and $c_1 = -c_3 = 1/\sqrt{2}$. CCN is not symmetrical, but if we assume that the orbital still has a node at the central carbon atom ($c_2 \cong 0.0$), we can use it to provide a simple interpretation of the magnetic hyperfine parameters. The two other coefficients can be estimated from the spin-orbit coupling constant

$$A = c_1^2\zeta_C + c_3^2\zeta_N, \quad [20]$$

where ζ_C and ζ_N are the 1-electron spin-orbit coupling constants for the C and N atoms. Using values of 42.1034 cm⁻¹ for A (this work) and of 29.0 and 73.3 cm⁻¹ for ζ_C and ζ_N , respectively (38), we calculate $c_1^2 = 0.706$ and $c_3^2 = 0.296$. The square of the coefficient on the N atom, c_3^2 , can also be estimated from the hyperfine parameters. Comparing the value

for $\langle r^{-3} \rangle_\ell$ for CCN and the N atom in Table 9, we obtain $c_3^2 = 0.274$, whereas the value for $\langle r^{-3} \rangle_s$ gives $c_3^2 = 0.287$; both are in good agreement with the value obtained from the spin-orbit coupling constant. The electron spin density at the nucleus, $\Psi(0)^2$, is much harder to interpret. It should be zero in the first order because the orbital has a node at the nucleus in both CCN and N; the small nonzero value which arises in reality is caused by spin-polarization effects.

It is not as easy to find a simple interpretation of the nuclear electric quadrupole parameters because this interaction depends on the distribution of all the charged particles in the molecule, not just that of the open-shell electrons. However, the parameter eQq_2 , which measures the deviation of the charge distribution from cylindrical symmetry, depends on the electrons in the π orbitals only. It is therefore not surprising that ratio of d to $|eQq_2|$ is almost constant for the three molecules in $^2\Pi$ states in Table 9 (5.079, 4.871, and 5.676 for CCN, NO, and NCO, respectively).

We were also able to learn quite a lot about the molecular Zeeman parameters from this study. In principle, these parameters provide some insight into the electronic structure of CCN. In particular, it can be seen from Table 6 that it has proved possible to determine separate values for the orbital and spin g -factors, g_L and g_S . This is because we have good quality data on the levels of both spin components $\tilde{X}^2\Pi_{1/2}$ and $\tilde{X}^2\Pi_{3/2}$ in a magnetic field. The value for g_S of 2.00197(12) implies a relativistic correction from the free-spin value of -1.7×10^{-4} , which is eminently reasonable (13). If we assume that the value for g_L of 1.00882(52) has a similar relativistic correction, the

resultant deviation from the classical value of unity can be interpreted as a nonadiabatic contribution of $+8.99 \times 10^{-3}$, arising from the differential admixture of excited ${}^2\Delta$ and ${}^2\Sigma$ states (39).

Several smaller g -factors have been used to model the effects of the external magnetic field. These g -factors can be estimated from their relationships with other molecular parameters, such as,

$$g_l = -\gamma/2B, \quad [21]$$

$$g_r^{e'} \cong -q/B, \quad [22]$$

$$(g_l' - g_r^{e'}) \cong (p + 2q)/2B, \quad [23]$$

$$\Delta g_L = -g_K'/\omega_2. \quad [24]$$

The experimental (and calculated) values for g_l , $g_r^{e'}$, $(g_l' - g_r^{e'})$, and Δg_L are 0.117×10^{-2} (0.114×10^{-2}), 0.1291×10^{-3} (-0.641×10^{-3}), 0.1559×10^{-2} (0.187×10^{-2}), and -0.1902×10^{-1} (-0.782×10^{-2}), respectively. Some of these values agree reasonably well while others do not.

The high sensitivity of intracavity LMR was demonstrated yet again by the detection of a low-frequency bending vibration of a short-lived free radical reported in this work. The intrinsic intensity of such a transition is at least two orders of magnitude smaller than that of the corresponding rotational (or electronic) transition. As a result of this study, the molecular parameters for CCN in its ${}^2\Pi$ ground state are considerably improved.

ACKNOWLEDGMENTS

This work was supported in part by NASA Contract W-19, 167. M.A. thanks the National Research Council and the National Institute of Standards and Technology for his postdoctoral fellowship.

REFERENCES

1. A. J. Merer and D. N. Travis, *Can. J. Phys.* **43**, 1795–1818 (1965).
2. T. J. Millar and E. Herbst, *Astron. Astrophys.* **288**, 561–571 (1994).
3. M. Kakimoto and T. Kasuya, *J. Mol. Spectrosc.* **94**, 380–392 (1982).
4. K. Hakuta and H. Uehara, *J. Chem. Phys.* **78**, 6484–6489 (1983).
5. C. R. Brazier, L. C. O'Brien, and P. F. Bernath, *J. Chem. Phys.* **86**, 3078–3081 (1987).
6. N. Oliphant, A. Lee, P. F. Bernath, and C. R. Brazier, *J. Chem. Phys.* **92**, 2244–2247 (1990).
7. K. Kawaguchi, T. Suzuki, S. Saito, E. Hirota, and T. Kasuya, *J. Mol. Spectrosc.* **106**, 320–329 (1984).
8. T. Suzuki, S. Saito, and E. Hirota, *J. Chem. Phys.* **83**, 6154–6157 (1985).
9. V. E. Bondybey and J. H. English, *J. Mol. Spectrosc.* **70**, 236–242 (1978).
10. M. E. Jacox, *J. Mol. Spectrosc.* **71**, 369–385 (1978).
11. K. Hakuta, H. Uehara, K. Kawaguchi, T. Suzuki, and T. Kasuya, *J. Chem. Phys.* **79**, 1094–1095 (1983).
12. M. Feher, C. Salud, and J. P. Maier, *J. Mol. Spectrosc.* **145**, 246–250 (1991).
13. D. A. Gillett and J. M. Brown, *Can. J. Phys.* **72**, 1001–1006 (1994).
14. Y. Ohshima and Y. Endo, *J. Mol. Spectrosc.* **172**, 225–232 (1995).
15. H. Kohguchi, Y. Ohshima, and Y. Endo, *J. Chem. Phys.* **106**, 5429–5438 (1997).
16. W. Gabriel, E.-A. Reinsch, and P. Rosmus, *Chem. Phys. Lett.* **231**, 13–17 (1994).
17. J. A. Pople, *Mol. Phys.* **3**, 16–22 (1960).
18. J. T. Hougen, *J. Chem. Phys.* **36**, 519–534 (1962).
19. R. J. Saykally, K. G. Lubic, A. Scalabrin, and K. M. Evenson, *J. Chem. Phys.* **77**, 58–67 (1982).
20. J. M. Brown, L. R. Zink, and K. M. Evenson, *Phys. Rev. A: Gen. Phys.* **57**, 2507–2510 (1998).
21. T. J. Sears, P. R. Bunker, A. R. W. McKellar, K. M. Evenson, D. A. Jennings, and J. M. Brown, *J. Chem. Phys.* **77**, 5348–5362 (1982).
22. G. Herzberg, "Spectra of Diatomic Molecules," Van Nostrand, Princeton, NJ, 1950.
23. J. M. Brown, *J. Mol. Spectrosc.* **68**, 412–422 (1977).
24. D. A. Gillett, Ph.D. thesis, University of Oxford, 1994.
25. J. M. Brown, E. A. Colbourn, J. K. G. Watson, and F. D. Wayne, *J. Mol. Spectrosc.* **74**, 294–318 (1979).
26. J. M. Brown, M. Kaise, C. M. L. Kerr, and D. J. Milton, *Mol. Phys.* **36**, 553–583 (1978).
27. S. A. Beaton and J. M. Brown, *J. Mol. Spectrosc.* **183**, 347–359 (1997).
28. R. A. Frosch and H. M. Foley, *Phys. Rev.* **88**, 1337–1349 (1952).
29. "Handbook of Chemistry and Physics," (D. R. Lide, Ed.), 74th ed., pp. 11–37, CRC Press, Ann Arbor, MI, 1993–1994.
30. C. A. Schmuttenmaer, R. C. Cohen, N. Pugliano, J. R. Heath, A. L. Cooksy, K. L. Busarow, and R. J. Saykally, *Science* **249**, 897–900 (1990).
31. H. Körsgen, K. M. Evenson, and J. M. Brown, *J. Chem. Phys.* **107**, 1025–1027 (1997).
32. T. C. Steimle, W.-L. Chang, D. F. Nachman, and J. M. Brown, *J. Chem. Phys.* **89**, 7172–7179 (1988).
33. T. D. Varberg, F. Stroth, and K. M. Evenson, *J. Mol. Spectrosc.* **196**, 5–13 (1999).
34. H. U. Suter, M.-B. Huang, and B. Engels, *J. Chem. Phys.* **101**, 7686–7691 (1988).
35. K. Kawaguchi, S. Saito, and E. Hirota, *Mol. Phys.* **55**, 341–350 (1985).
36. H. E. Radford and K. M. Evenson, *Phys. Rev.* **168**, 70–74 (1968).
37. R. H. Lambert and F. M. Pipkin, *Phys. Rev.* **129**, 1233–1239 (1963).
38. H. Lefebvre-Brion and R. W. Field, "Perturbations in the Spectra of Diatomic Molecules," p. 214 Academic Press, Orlando, FL, 1988.
39. J. M. Brown and H. Uehara, *Mol. Phys.* **24**, 1169–1174 (1972).